minerals

MDPI

Article

Lithium-Rich Deposits in the Liangshan Formation during the Permian in the Upper Yangtze Plate, China

Yin Gong [1,2], Chun-Yao Liu [3,*], Yin Liu [1], Li Lei [1], Meng Xiang [1], Bo Yang [1], Zhou Zhou [1], Yang Zhang [1], Xiang-Rong Yang [4], Lei Yan [1] and Yuan Xiong [1]

1 The Seventh Geological Brigade of Hubei Geological Bureau, Yichang 443100, China; gongyincug@163.com (Y.G.)
2 Expert Workstation of the Seventh Geological Brigade of Hubei Geological Bureau, Yichang 443100, China
3 Third Institute of Oceanography, Ministry of Natural Resources of China, Xiamen 361005, China
4 School of Geosciences, Yangtze University, Wuhan 430100, China
* Correspondence: liu-chunyao@outlook.com or liuchunyao@tio.org.cn

Abstract: With the increasing demand for lithium (Li) resources in industry, there has been new attention on clay-type lithium-rich deposits recently. In this study, a Li-rich clay deposit with a Li_2O content up to 0.3% in the Liangshan Formation in the upper Yangtze, South China Block was demonstrated. We analysed the mineralogy and element geochemistry of the samples from the Liangshan Formation and its underlying and overlying layers. Kaolinite (average 53%, up to 93%) was the major mineral in the samples from the Liangshan Formation. The Li concentrations increased with increasing kaolinite compositions and Al_2O_3 concentrations. Furthermore, based on the geochemical indicators, it was suggested that the clay formation and Li enrichment were related to the weathering processes of the bottom impure limestone under the hot and wet climate, and the sedimentary processes in the anoxic, still, and flat land–sea interaction area in the Upper Yangtze. The Li was probably sourced from the bottom impure limestone during the weathering stage. The samples from the Liangshan Formation also showed REE enrichment from 117 to 729 μg/g.

Keywords: lithium-rich deposit; weathering; clay formation; Permian; lithium resource

check for updates

Citation: Gong, Y.; Liu, C.-Y.; Liu, Y.; Lei, L.; Xiang, M.; Yang, B.; Zhou, Z.; Zhang, Y.; Yang, X.-R.; Yan, L.; et al. Lithium-Rich Deposits in the Liangshan Formation during the Permian in the Upper Yangtze Plate, China. *Minerals* **2024**, *14*, 735. https://doi.org/10.3390/min14070735

Academic Editors: Maria Economou-Eliopoulos and Harald G. Dill

Received: 2 June 2024
Revised: 7 July 2024
Accepted: 17 July 2024
Published: 22 July 2024

Copyright: © 2024 by the authors. Licensee MDPI, Basel, Switzerland. This article is an open access article distributed under the terms and conditions of the Creative Commons Attribution (CC BY) license (https://creativecommons.org/licenses/by/4.0/).

1. Introduction

Lithium (Li) is one of the essential resources in industry, especially for Li-ion batteries and materials containing Li [1,2]. Because of the high demand for products containing Li, prospecting and exploration of Li resources are currenly regarded as a key topic [3–5]. The Li resources are mainly from Li-rich pegmatite deposits (e.g., Greenbushes, Australia; Jiajika, China) and Li-rich brine deposits (e.g., Uyuni, Bolivia; Atacama, Chile) [5,6]. While, moreLi-rich clay deposits have recently been discovered, which may become an important new Li resource for the industry [3]. According to their provenance, one type is owed to the alteration of volcanic rocks by hydrothermal fluid (e.g., Sonora, Mexico; Jadar, Serbia; McDermitt, USA) [7,8] and the other type is bauxite-related Li-rich deposits formed by the low-temperature weathering at the Earth's surface [3].

Specifically, some Li-rich clay deposits that are related to the weathering of the underlying carbonate were discovered in southern China [9]. For example, Li-rich bauxite from the Dazhuyuan Formation in the lower Permian was discovered in the Wuchuan-Zheng'an-Daozhen area, Guizhou Province, where the average level of Li_2O ranges from 0.75 to 1.75% [10,11]. Also, Li-rich bauxite deposits from the early Permian have been reported in the Daoshitou Formation in central Yunnan [9,12] and the Liangshan Formation in the Panzhihua area, Sichuan [13]. The Li_2O composition of these two deposits can be up to 1.1% [9,13]. In addition, in the Pinggou area, Guangxi Province, a Li-rich layer in the Heshan Formation during the middle Permian, with Li_2O up to 1.1%, was reported and the Li was thought to be enriched in the kaolinite [3,14].

Given the wide distribution of Li-rich clay layers during the Palaeozoic in southern China, it is worth exploring more areas with similar stratigraphy groups and environmental conditions in southern China. This study aims to provide a new case of a clay-type Li-rich deposit and a new view on the supply of Li resources. In this study, we investigated a Li-rich clay deposit (maximum Li_2O content of 0.3%) during the early Permian in western Hubei, China. The geochemical characteristics and mineralogy of two trail trenches and a drill core were analysed. In addition, we discussed the Li enrichment pattern and mineral deposit mechanism. The mineralisation of the Li-rich clay deposit reported in this study implies the potential for large-scale clay-related Li-rich deposits, which may be a new Li resource.

2. Geological Setting and Sampling

The Li-rich deposit (110°30′59″ E, 30°43′25″ N) is from the Liangshan Formation in the South China Block and the deposit was developed during the early Permian (Figure 1).

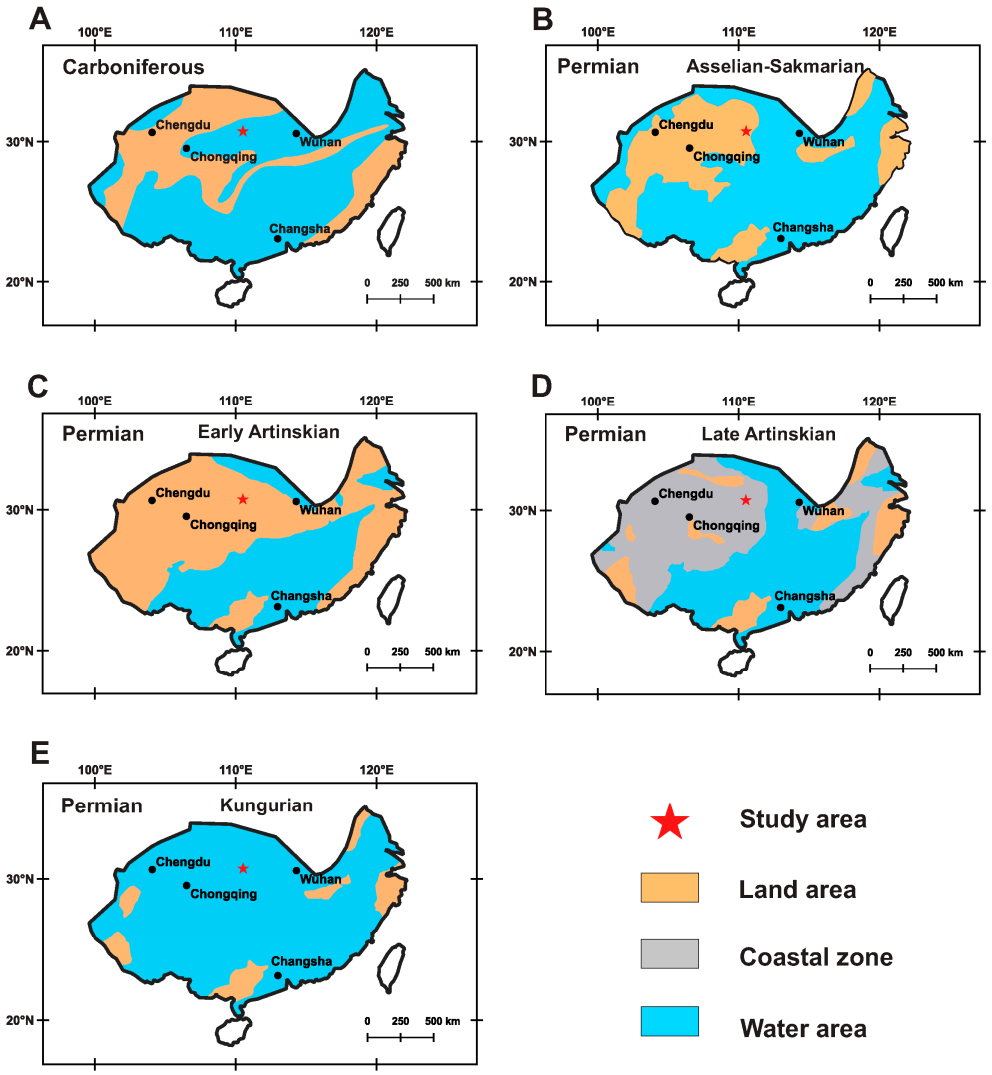


Figure 1. The reconstructed palaeographic maps of the South China Block during the late Carboniferous and early Permian. The subfigure (**A**) is modified from [15], and (**B**–**E**) are modified from [16].

2.1. The Paleogeographic Evolution of the Study Area during the Late Carboniferous to Early Permian

During the late Carboniferous to early Permian, the South China Block (SCB) was an isolated and stable block drifting southward to the equator [16–18]. The SCB was bordered

by the Paleo-Tethys and Panthalassa Oceans [16]. The SCB was formed by the Yangtze Province and Southeast Province colliding along the Jiangnan Orogenic Belt [15], and the Li deposit in this study is located in the upper Yangtze sub-province. During the late Carboniferous around 300 Mya ago, the SCB experienced a major transgression event, so the most upper Yangtze sub-province was located in the shallow marine environment and developed a thick limestone deposit (i.e., the Huanglong Formation) (Figure 1A) [15,19,20]. During the early Permian (i.e., Cisuralian), due to the regression and tectonic uplift at the SCB, most of the Yangtze area was exposed as land at the early Artinskian Stage (Figure 1C) [15,16,21]. However, due to the large transgression during the late Artinskian to Kungurian, most of the area at the SCB was in the coastal environment or shallow marine environment (Figure 1D) [15,16]. Specifically, the study area was the land exposed at the early Artinskian Stage, located in a coastal zone at the late Artinskian Stage, and located in a shallow marine at the Kungurian Stage (Figure 1). Thus, in the study area, a group of coal-bearing clastic rocks (i.e., the Liangshan Formation) deposited at the land–sea interaction sedimentary environment after a depositional hiatus, and a layer of organic-rich dark limestone, known as the Qixia (Chihsia) Formation, overlayed the clastic rock deposit [15,16,21].

2.2. The Stratigraphic Succession of the Li-Rich Deposit in the Study Area

The Li-rich deposits in this study are from Changyang, west Hubei area (Figure 1). In the study area, the stratigraphic succession from the late Carboniferous to the early Permian includes the Huanglong Formation, Liangshan Formation, and the Qixia (Chihsia) Formation. The Huanglong Formation is a thick grey micritic limestone deposit, which is a parallel unconformity covered by the Liangshan Formation (Figure 2) [15]. The Liangshan Formation is composed of clastic rocks, including fine sandstone, siltstone, argillaceous and carbonaceous mudstone, and kaolinite clay rock with a coal streak (Figure 2) [15,16]. It is notable that the Li-rich deposit is from the Liangshan Formation. The Qixia Formation overlaying the Liangshan Formation is composed of the ultra-thick organic-rich dark-grey micritic limestone with chert nodules and fossils (e.g., coral, Fuzulinid, Brachiopoda, Bivalvia) (Figure 2) [16].

2.3. Sample Collection

A drill core and two trail trenches were collected and analysed in this study (Figure 2). The drill core (ZK1402) was located in the central area of the Li-rich deposit. A group of 56 mm diameter cores were obtained using diamond drill bits. After removing the surface dust, seven samples from the drill core were collected from a depth of 210 to 222 m for analyses, which corresponds to the Liangshan Formation. The trail trenches are located at the western rim (TC08) and southern rim (BT06) of the south part of the deposit area. There were seven samples from the TC08 crossing of the Liangshan Formation and 17 samples deposited at the Huanglong Formation, Liangshan Formation, and Qixia (Chihsia) Formation were collected from the BT06 trail trench.

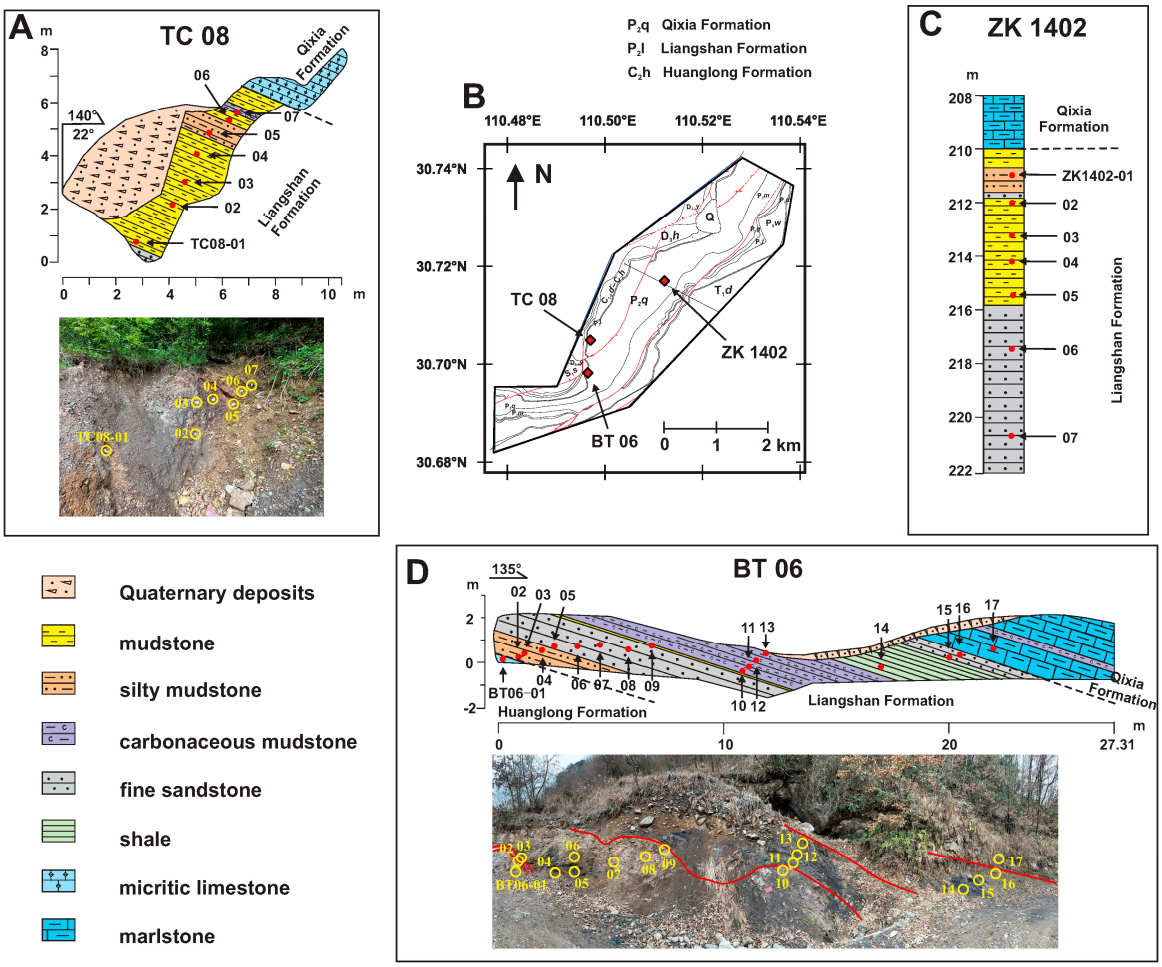


Figure 2. The sampling maps and field photos. Subfigure (**B**) is the Li-rich deposit area, and the details of formation symbols (e.g., P_2l) are described in the supplementary material (Table S1). In Subfigure B, the black lines are stratigraphic boundaries and the red lines represent structural lines. The subfigures (**A**,**C**,**D**) are the maps and field photos of sampling points trail trench TC08, drill core ZK1402, and trail trench BT06, respectively. The legends for subfigure (**A**,**C**,**D**) are at the left bottom. The yellow circles in the field photos are sample IDs and the red lines in the field photos are the boundary between the layers.

3. Methods

3.1. Element Composition Analyses

The element compositions of the samples from TC08 and ZK1402 were analysed by the Wuhan SampleSolution Analytical Technology Co., Ltd. (Wuhan, China). The samples were crushed, ground, and homogenised. For major element compositions (i.e., SiO_2, Al_2O_3, $T(Fe_2O_3)$, MgO, CaO, Na_2O, K_2O, TiO_2, P_2O_5, and MnO), an aliquot powder of each sample was dissolved with lithium tetraborate ($Li_2B_4O_7$) at 1080 °C and cast into a mold with a flat bottom to make the fusion beads. Then, the major element compositions were determined by X-ray fluorescence (XRF, Rigaku ZSX Primus II, Tokyo, Japan). The relative standard deviation (RSD) of the XRF analysis was better than 2%. For trace element concentrations (i.e., Li, Ga, Nb, Ta, Ba, Ni, Sr, V, Zr, Hf, and REE), a weighted powder of each sample (around 0.1g) was dissolved with hydrogen fluoride (HF), hydrochloric acid (HCl), and nitric acid (HNO_3) in the Teflon crucible. Then the trace element concentrations were determined by inductively coupled plasma mass spectrometry (ICP-MS, Agilent 7700e, USA). The relative standard deviation (RSD) of the ICP-MS analysis was better than 6%. The FeO contents of samples were determined by the potassium dichromate titration

method. The loss on ignition (LOI) was the difference between the sample weights after ignition at 110 °C in the muffle furnace and the weight before ignition.

The element compositions of the samples (except BT06-08) from BT06 were analysed at the Hubei Geological Research Laboratory (Wuhan, China). The major element compositions (i.e., SiO_2, Al_2O_3, T(Fe_2O_3), MgO, CaO, Na_2O, K_2O, TiO_2, P_2O_5, and MnO) and the concentrations of Hf and Zr were analysed by XRF (SHIMADZU XRF-1800) after fusing the sample powders with $Li_2B_4O_7$. The concentrations of Li, Ba, Ni, Sr, and V were analysed by inductively coupled plasma optical emission spectroscopy (ICP-OES, Thermo Scientific™ iCAP™ 7400) and the concentrations of REE, Ga, Nb, and Ta were analysed by ICP-MS (Thermo Scientific™ XSERIES 2) after dissolving the sample powder with HF–HCl–HNO_3. The relative standard deviation (RSD) of the ICP-OES and ICP-MS analyses was better than 6%. The FeO contents of samples were determined by the potassium dichromate titration method. The loss on ignition (LOI) was the difference between the sample weights after ignition at 110 °C in the muffle furnace and the weight before ignition.

To obtain the REE patterns, the REE concentrations were normalized by CI chondrite [22]. The chemical index of alteration (CIA) of the samples from the Liangshan Formation was calculated using the concentrations of major elements (Equation (1)) to show the chemical degree [23].

$$CIA = [Al_2O_3/(Al_2O_3 + CaO^* + Na_2O + K_2O] \times 100 \quad (1)$$

The CaO* is the CaO concentration in silicates.

3.2. Mineralogy Identification

The mineralogy identifications were conducted at the Hubei Geological Research Laboratory (Wuhan, China). The 15 samples from the Liangshan Formation at BT06 and all samples at TC08 and ZK1402 were crushed to less than 80 μm using an agate mortar and pestle for X-ray diffraction (XRD) analysis. The XRD analysis was conducted using the Bruker D8 FOCUS, Berlin, Germany. The diffraction angle was from 3 to 70° (2θ) with a step size of 0.01°. The minerals were distinguished based on the powder diffraction file (PDF), and the quantitative analyses were applied using Siroquant 4.0. Five samples at BT06 were impregnated in epoxy and made into standard thin sections. The rock structure, rock texture, and mineral composition of the samples were observed using the polarizing microscope (ZEISS Axio Scope, Germany).

To investigate the crystallinity of the kaolin deposits, the Hinckley index (H.I.) of the samples that consist of more than 50% kaolinite (i.e., samples BT06-09 to 13, TC08-01 to 04, and ZK1402-02 to 05) were calculated according to the peak heights of $(1\bar{1}0)$ and $(11\bar{1})$ at diffraction angles of (2θ) ~ 20.4° and ~21.3° on XRD patterns (Figure S1) [24,25].

4. Results

4.1. Mineral Compositions

The samples from the Liangshan Formation were mainly composed of clay minerals and quartz, and kaolinite was the main type of clay mineral (Table 1). For the BT06 trail trench, the samples BT06-02 and 03 were composed of 4%–9% quartz and more than 50% clay minerals. The BT06-02 also had a relatively high gibbsite content (~37%). While the BT06-04 to 08 was dominated by quartz, which took up 58%–82%. However, there was a shift of the primary mineral from quartz to kaolinite from the lower to upper Liangshan Formation. The contents of clays of the samples BT06-09 to 14 ranged from 79% to 98% (Figure 3). The main clay was kaolinite, which takes up more than 77% of clay minerals and more than 60% of the total minerals in samples BT06-09 to 14. Furthermore, some samples of BT06 trail trench had feldspar, chlorite, smectite, illite-smectite, illite, hematite, goethite, and pyrophyllite (Table 1). Similarly, for trail trench TC08 and drill core ZK1402, the main minerals in most samples were kaolinite, with the content ranging from 16% to 93%. Some samples had relatively high levels of quartz, illite, chlorite, pyrophyllite, or feldspar (Table 1).

Table 1. The mineral compositions of the samples.

Samples	Quartz	Chlorite	Illite	Kaolinite	Illite-Smectite	Smectite	Pyrophyllite	Gibbsite	Diaspore	Calcite	Feldspar	Hematite	Goethite	Anatase	H.I.
	%	%	%	%	%	%	%	%	%	%	%	%	%	%	
BT06-16	32	15	33		6	7				4			3		
BT06-15	79	5	2	6	2	2	3						1		
BT06-14		12	3	61	2		21						1		0.9
BT06-13		3	2	88	2	3					2				1.3
BT06-12		14		73	5		8								1.3
BT06-11		7		84	2		4				3				1.2
BT06-10		13		72	4		8				3				0.7
BT06-09	7	3	3	69	2	4	7				2		3		0.8
BT06-07	82	2	1	8	1	2	3						1		
BT06-06	65	4	3	10	3	3	9						3		
BT06-05	70	4	4	9	4	4	5								
BT06-04	58	6	4	11	5		6					5	5		
BT06-03	9	16	11	24	28		6					6			
BT06-02	4	8		32	6	7	4	37					2		
ZK1402-01	37	12	28	16							3		3	1	
ZK1402-02		4		90							3			3	1.1
ZK1402-03		4		93							1			2	1.3
ZK1402-04		4		91			2				2			1	1.3
ZK1402-05		5	2	89							2			2	0.3
ZK1402-06	51	2	2	31			10		3					1	
ZK1402-07			3	18			29				50				
TC08-07	15	9	38	24			7				5			2	
TC08-06	14	15	32	26			4				3		4	2	
TC08-05	24	6	11	47			6				3		3		
TC08-04		9		81			2				6			2	1.1
TC08-03		9		89							1			1	1.3
TC08-02		11		86							2			1	1.3
TC08-01		3		93			1				2			1	1.1

The mineral compositions were quantified using XRD pattern software Siroquant 4.0. The H.I. of samples that consist of more than 50% kaolinite was calculated (Section 3.2, Figure S1).

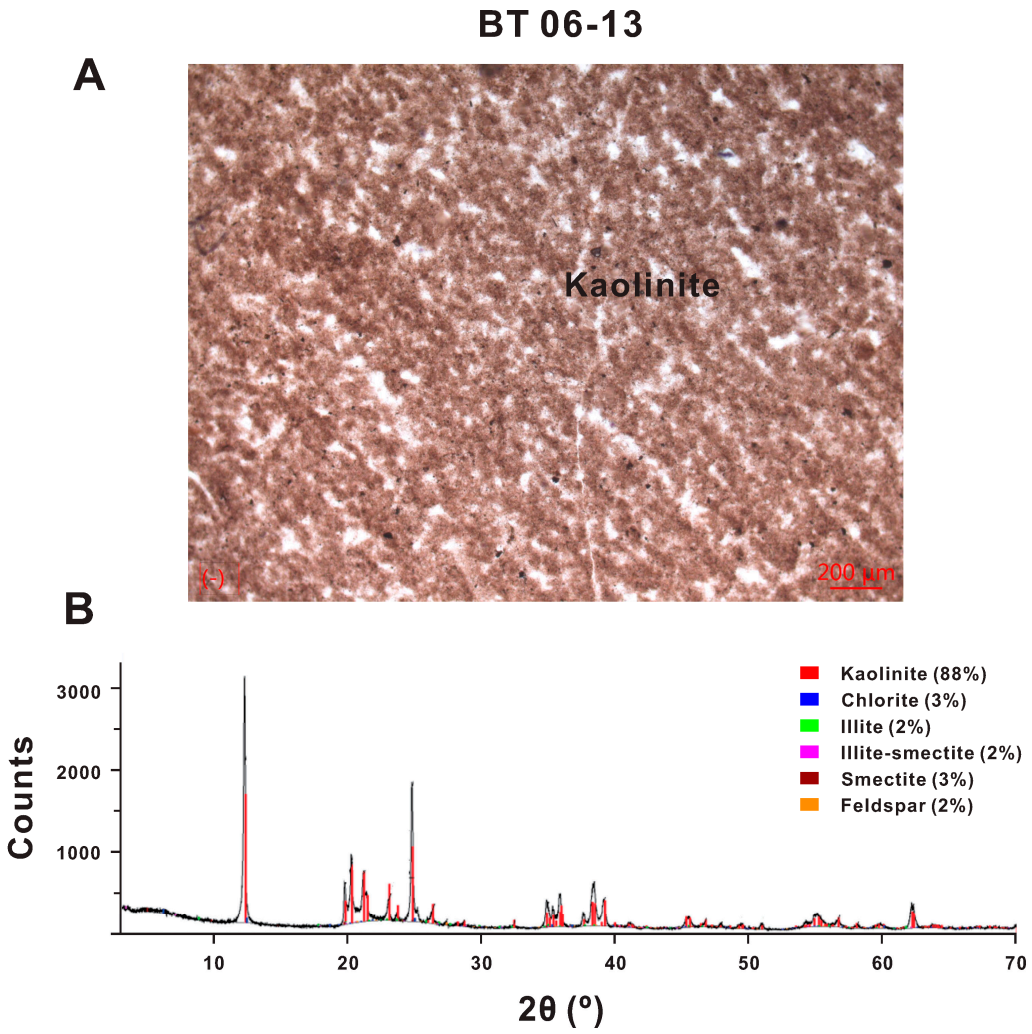


Figure 3. The image of the thin section under the polarizing microscope and XRD patterns of sample BT06-13 from the Liangshan Formation. The image of the thin section was observed through cross-polarized light. (**A**) The image of the thin section of sample BT06-13 under the polarizing microscope. (**B**) The XRD patterns of sample BT06-13.

4.2. Element Concentrations

The element concentrations are shown in Tables 2–4.

Table 2. The major element concentrations, LOI, and CIA of the samples.

Samples	SiO_2	Al_2O_3	MgO	Na_2O	CaO	K_2O	Fe_2O_3	FeO	TiO_2	LOI	CIA
	%	%	%	%	%	%	%	%	%	%	
BT06-17	2.6	1.5	0.54	0.083	53.1	0.20	0.86	0.18	0.061	41.0	
BT06-16	51.0	24.5	1.67	0.37	1.20	3.25	7.37	0.42	1.00	8.8	0.84
BT06-15	82.7	9.7	0.54	0.19	0.32	0.56	1.12	0.25	0.68	3.5	0.90
BT06-14	36.3	26.9	1.33	0.18	2.47	0.59	0.14	0.35	0.97	30.4	0.89
BT06-13	44.8	37.4	0.14	0.12	0.28	0.20	0.50	0.32	1.25	14.6	0.98
BT06-12	34.0	28.1	0.44	0.13	3.39	0.25	2.27	0.88	1.04	29.1	0.88
BT06-11	43.9	36.2	0.30	0.15	0.40	0.16	2.34	0.22	1.55	14.4	0.98
BT06-10	40.1	32.5	0.37	0.19	1.70	0.38	0.20	0.28	1.58	22.2	0.93
BT06-09	47.1	32.6	0.16	0.15	0.28	0.23	3.89	0.18	3.15	11.7	0.98
BT06-07	85.8	8.0	0.11	0.11	0.14	0.27	1.59	0.18	0.48	2.9	0.94
BT06-06	74.2	7.1	0.13	0.15	0.36	0.41	10.92	0.35	0.78	5.2	0.89
BT06-05	84.1	5.9	0.14	0.15	0.36	0.42	2.56	0.45	0.72	4.8	0.86

Table 2. *Cont.*

Samples	SiO_2	Al_2O_3	MgO	Na_2O	CaO	K_2O	Fe_2O_3	FeO	TiO_2	LOI	CIA
	%	%	%	%	%	%	%	%	%	%	
BT06-04	51.6	12.8	0.15	0.27	0.34	0.56	25.29	0.62	0.74	7.1	0.92
BT06-03	41.2	26.4	0.55	1.13	0.76	1.73	18.68	0.38	1.18	7.7	0.88
BT06-02	38.6	40.1	0.065	0.17	0.22	0.16	2.81	0.15	0.16	17.0	0.99
BT06-01	1.1	1.3	0.23	0.073	55.4	0.051	0.24	0.083	0.052	41.8	
ZK1402-01	62.9	19.2	1.03	0.29	0.28	2.59	5.18	0.15	0.89	6.1	0.86
ZK1402-02	44.0	38.0	0.06	0.05	0.12	0.06	1.41	0.20	1.89	13.9	0.99
ZK1402-03	44.5	38.8	0.08	0.08	0.11	0.15	0.51	0.10	1.46	13.7	0.99
ZK1402-04	42.4	36.5	0.16	0.07	0.20	0.26	3.90	0.10	1.81	13.9	0.99
ZK1402-05	44.8	38.1	0.18	0.29	0.18	0.46	0.85	0.05	1.68	12.9	0.98
ZK1402-06	75.2	14.1	0.16	0.09	0.13	0.51	3.31	0.10	0.90	5.3	0.95
ZK1402-07	78.7	10.8	0.19	0.29	0.14	0.76	4.75	0.10	0.87	3.6	0.90
TC08-07	54.1	28.9	1.12	0.45	0.47	3.64	0.82	0.10	1.22	8.3	0.86
TC08-06	49.9	27.9	0.92	0.40	0.44	3.34	6.81	0.10	1.23	8.2	0.87
TC08-05	65.1	19.3	0.20	0.15	0.19	0.70	5.10	0.05	1.48	6.4	0.95
TC08-04	43.0	36.7	0.34	0.16	0.32	0.66	3.70	0.10	1.59	13.2	0.97
TC08-03	43.1	39.5	0.22	0.09	0.17	0.17	0.71	0.05	1.36	13.8	0.99
TC08-02	43.3	39.5	0.22	0.08	0.17	0.20	0.59	0.05	1.27	13.9	0.99
TC08-01	44.5	38.3	0.05	0.07	0.11	0.12	0.79	0.05	1.71	13.8	0.99

The relative standard deviations (RSDs) of major element concentrations were better than 2%.

Table 3. The concentrations of Li, Ga, Nb, Ta, Ba, Ni, Sr, V, Zr, and Hf in the samples.

Samples	Li	Ga	Nb	Ta	Ba	Ni	Sr	V	Zr	Hf
	μg/g	μg/g	μg/g	μg/g	μg/g	μg/g	μg/g	μg/g	μg/g	μg/g
BT06-17	20.9	1.81	1.34	0.120	28.4	7.95	309	21.2	19.3	0.397
BT06-16	117	27.4	20.0	1.76	248	34.4	348	226	267	7.72
BT06-15	51.6	14.7	12.5	0.979	76.5	21.1	282	64.0	1050	38.5
BT06-14	366	41.2	16.1	1.27	138	19.4	272	169	394	14.4
BT06-13	430	23.4	37.2	2.61	34.1	28.1	72.0	138	471	18.4
BT06-12	407	36.8	17.9	1.84	87.7	42.1	155	272	420	14.9
BT06-11	496	30.7	28.4	2.25	38.2	50.5	106	164	854	31.5
BT06-10	417	37.1	30.2	2.26	95.3	22.1	160	220	618	23.3
BT06-09	129	44.2	62.1	4.66	43.6	19.6	122	187	3540	133
BT06-07	16.1	9.88	9.11	0.768	45.8	3.39	89.4	95.3	536	19.2
BT06-06	12.7	14.6	13.9	1.13	65.2	1.77	126	234	751	23.0
BT06-05	10.2	11.7	13.1	1.01	73.3	1.48	126	138	744	26.3
BT06-04	17.7	16.0	13.1	1.02	82.8	3.42	227	221	562	12.5
BT06-03	20.1	31.9	24.3	1.84	138	13.9	748	145	544	14.2
BT06-02	44.1	4.63	4.46	0.45	39.7	286	99.7	49.5	69.5	2.73
BT06-01	24.7	1.11	1.18	0.17	10.1	8.24	265	6.75	26.6	0.93
ZK1402-01	124	23.8	19.9	1.52	4930	43.4	705	191	468	12.9
ZK1402-02	539	34.6	45.7	3.22	10.4	36.5	50.5	120	714	19.9
ZK1402-03	739	26.5	44.4	2.97	20.1	29.3	64.1	188	621	17.5
ZK1402-04	757	37.4	43.2	3.20	32.4	84.2	106	351	1070	29.6
ZK1402-05	705	40.9	38.2	2.73	54.7	42.3	207	174	691	19.9
ZK1402-06	59.5	16.5	19.8	1.54	64.9	30.9	149	119	964	25.5
ZK1402-07	18.8	16.3	18.9	1.53	96.6	3.46	387	126	859	23.2
TC08-07	222	36.5	29.2	2.15	195	14.6	436	279	245	7.30
TC08-06	161	38.0	27.4	2.09	177	46.6	367	256	303	8.81
TC08-05	243	25.4	39.1	4.02	49.8	18.5	145	215	5980	175
TC08-04	817	59.4	34.9	2.58	82.3	41.0	134	167	407	11.9
TC08-03	1970	23.6	41.0	2.45	19.0	55.4	64.7	204	518	15.0
TC08-02	1810	22.0	29.7	1.99	28.8	88.2	72.3	166	522	14.8
TC08-01	462	34.6	38.8	2.82	16.7	28.2	38.0	153	895	24.2

The relative standard deviations (RSDs) of trace element concentrations were better than 6%.

Table 4. The REE concentrations of the samples.

Samples	La	Ce	Pr	Nd	Sm	Eu	Gd	Tb	Dy	Ho	Er	Tm	Yb	Lu	∑REE
	μg/g	μg/g	μg/g	μg/g	μg/g	μg/g	μg/g	μg/g	μg/g	μg/g	μg/g	μg/g	μg/g	μg/g	μg/g
BT06-17	15.3	34.7	4.17	16.2	2.9	0.50	2.4	0.33	1.4	0.25	0.65	0.097	0.55	0.076	79.4
BT06-16	54.6	115	16.2	59.1	10	1.6	7.0	0.97	4.5	0.90	2.9	0.50	3.2	0.47	277
BT06-15	52.9	117	15.1	56.7	10	1.5	9.9	1.9	9.4	1.8	4.6	0.71	3.9	0.53	287
BT06-14	73.3	114	12.5	31.4	2.6	0.47	5.2	0.74	4.5	1.1	3.4	0.64	3.8	0.52	254
BT06-13	61.1	102	11.4	30.2	2.6	0.41	4.7	0.74	4.6	0.99	3.1	0.54	3.2	0.44	226
BT06-12	111	218	18.8	47.2	6.1	1.0	12	2.5	17	4.0	12	2.0	11	1.6	463
BT06-11	73.6	109	11.7	27.7	2.7	0.48	4.9	0.85	5.8	1.3	4.4	0.79	4.6	0.65	248
BT06-10	107	241	20.4	48.5	4.8	0.79	8.8	1.4	8.7	1.9	6.0	1.0	6.0	0.84	457
BT06-09	60.7	101	13.5	48.2	8.2	1.3	7.9	1.7	12	2.6	8.3	1.5	9.1	1.3	277
BT06-07	42.5	82.5	11.1	37.7	4.5	0.49	4.3	0.51	2.4	0.49	1.7	0.29	1.8	0.26	191
BT06-06	71.7	137	15.7	45.8	4.9	0.50	5.7	0.70	3.7	0.83	2.8	0.51	3.2	0.45	293
BT06-05	80.5	172	18.9	57.9	5.7	0.61	7.2	0.91	4.9	1.1	3.3	0.58	3.4	0.47	357
BT06-04	40.1	77.8	8.35	26.8	3.0	0.41	3.4	0.50	2.9	0.65	2.2	0.43	2.5	0.36	169
BT06-03	27.7	62.3	7.93	27.9	3.4	0.55	3.4	0.59	3.5	0.76	2.5	0.47	2.8	0.40	144
BT06-02	12.5	77.8	5.38	25.0	7.4	1.2	5.5	1.1	5.4	1.00	2.8	0.52	3.2	0.44	149
BT06-01	11.0	18.3	2.65	12.0	2.8	0.59	2.7	0.50	2.5	0.48	1.2	0.18	1.0	0.15	56.1
ZK1402-01	67.6	180	15.9	56.4	10	1.9	6.9	1.0	5.8	1.2	3.2	0.48	3.4	0.56	355
ZK1402-02	20.0	41.0	4.96	19.6	4.1	0.85	4.7	1.0	7.3	1.7	4.9	0.75	5.2	0.82	117
ZK1402-03	37.5	77.9	7.39	21.8	3.0	0.63	3.5	0.91	6.8	1.5	4.2	0.63	4.4	0.71	171
ZK1402-04	63.9	135	12.7	39.2	7.4	1.5	9.4	2.3	17	3.9	11	1.7	12	1.8	319
ZK1402-05	82.0	127	10.5	29.5	4.0	0.90	4.2	1.0	8.3	2.1	6.2	0.93	6.4	1.0	284
ZK1402-06	65.3	108	10.5	36.6	5.0	0.66	3.3	0.55	3.7	0.82	2.7	0.44	3.3	0.57	241
ZK1402-07	50.8	98.3	10.2	38.4	5.8	0.60	2.9	0.45	3.1	0.74	2.4	0.38	2.8	0.49	217
TC08-07	65.8	151	13.5	49.1	8.2	1.3	4.9	0.83	5.1	1.2	3.2	0.48	3.5	0.56	309
TC08-06	60.4	137	12.6	49.9	9.9	1.5	6.2	1.0	6.0	1.3	3.5	0.52	3.6	0.59	294
TC08-05	94.5	179	18.9	67.3	9.3	1.2	7.5	1.4	9.1	2.2	7.2	1.3	9.7	1.8	411
TC08-04	185	321	35.6	115	20	3.3	16	2.2	12	2.5	6.8	1.0	7.1	1.1	729
TC08-03	39.1	85.2	9.78	34.5	7.1	1.2	7.0	1.4	8.8	1.9	4.9	0.71	4.9	0.75	207
TC08-02	33.4	69.8	7.93	28.4	5.0	0.83	5.4	1.2	7..4	1.6	4.4	0.66	4.5	0.72	171
TC08-01	29.5	52.0	5.65	21.6	4.4	0.70	4.9	1.1	7.5	1.7	5.0	0.78	5.3	0.85	141

The relative standard deviations (RSDs) of REE element concentrations were better than 6%.

In trail trench BT06, the samples from the Huanglong Formation (BT06-01) and the Qixia Formation (BT06-17) consist of ~55% CaO and ~41% LOI, both of which are higher than the CaO content (0.1%–3%) and LOI content (3%–30%) of the samples from the Liangshan Formation (i.e., BT06-02 to 16) (Table 2). Correspondingly, the SiO_2 and Al_2O_3 contents of samples BT06-01 and 17 are lower than samples BT06-02 to 16. To be specific, the content of SiO_2 and Al_2O_3 in samples BT06-02 to 16 range from 34%–86% and 6%–40%, respectively (Figure S2). The Fe_2O_3 (i.e., total Fe) content ranges from 0.2%–25%, while the FeO only takes up 0.1%–0.9% of the samples from BT06. The contents of total alkali and alkaline earth elements (i.e., MgO, Na_2O, CaO, and K_2O) are 0.6% to 5%.

In drill core ZK1402, the LOI contents in samples are 4% to 14% (Table 2). The major element composition of samples from ZK1402 is SiO_2, with content ranging from 63% to 79%, followed by Al_2O_3 (11%–39%). Similarly, the samples from trail trench TC08 are dominated by SiO_2 (43%–65%) and Al_2O_3 (19%–40%), and the LOI contents are 6% to 14%.

The Li concentrations in the samples from the Huanglong Formation (i.e., sample BT06-01) and the Qixia Formation (i.e., sample BT06-17) are 20.9 and 24.7 μg/g, respectively (Table 3). While the Li concentrations in samples from the Liangshan Formation in this study range widely from 10.2 to 1970 μg/g (Figure S2). Moreover, the samples from TC08 have relatively higher Li concentrations (161–1970 μg/g) than ZK1402 (18.8–757 μg/g) and BT06 (10.2–496 μg/g) (Table 3, Figures 4–6). Generally, the cut grade of Li is 0.1% Li_2O, i.e., 467 μg/g. The samples that have higher levels of Li than the cut grade had a Li concentration of 1531 μg/g (average) ± 624 μg/g (standard deviation) at TC08 and 685 μg/g (average) ± 100 μg/g (standard deviation) at ZK1402. The ΣREE (i.e., total REE concentration) of the samples from the Liangshan Formation ranges from 117 to 729 μg/g (Figure S2), while the ΣREEs in the samples BT06-01 and BT06-17 are 56.1 and 79.4 μg/g, respectively (Table 4).

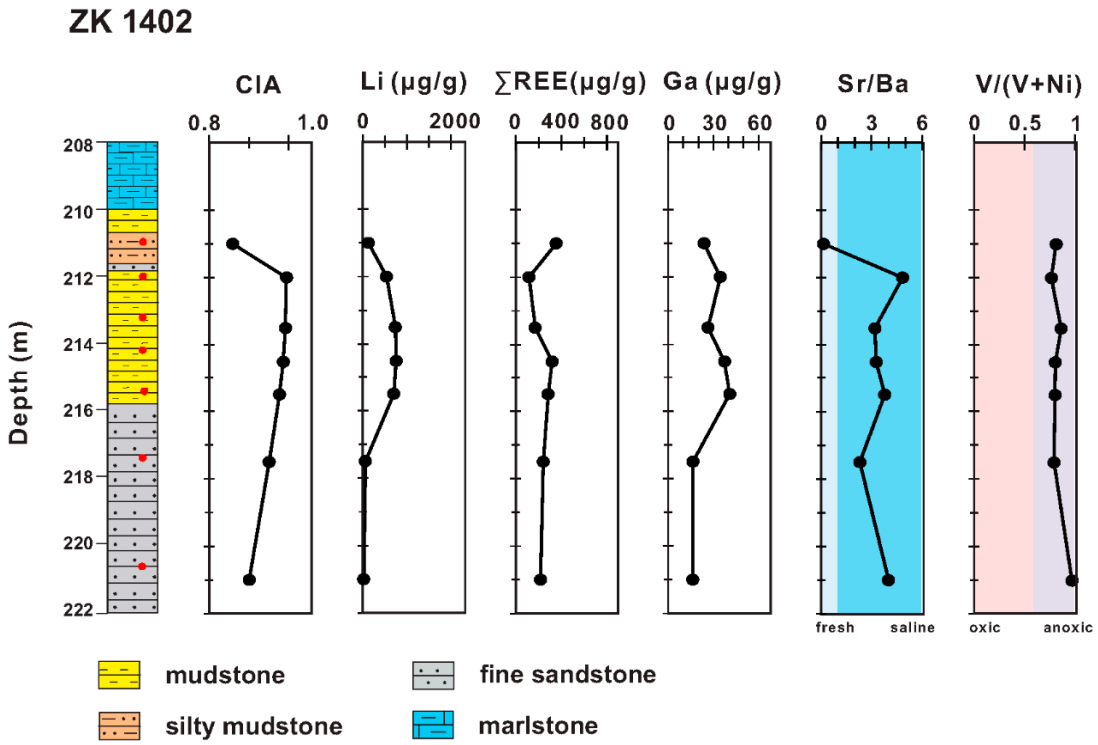


Figure 4. The geochemistry of drill core ZK1402. The red dots are the sample ZK1402-01 to 07 from up to bottom.

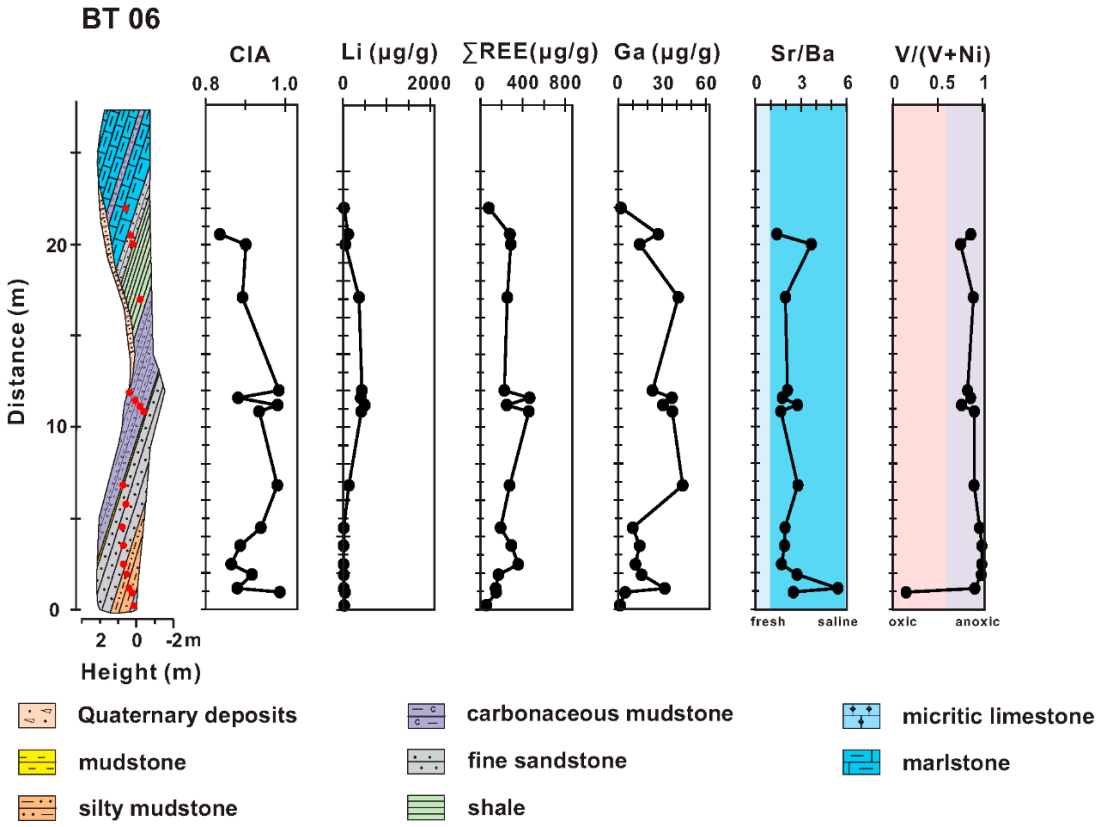


Figure 5. The geochemistry of trail trench BT06. The red dots are the samples BT06-01 to 17 from bottom to up. The samples from the bottom (BT06-01 from the Huanglong Formation) and top (BT06-17 from the Qixia Formation) were not shown (see the data in Tables 2–4).

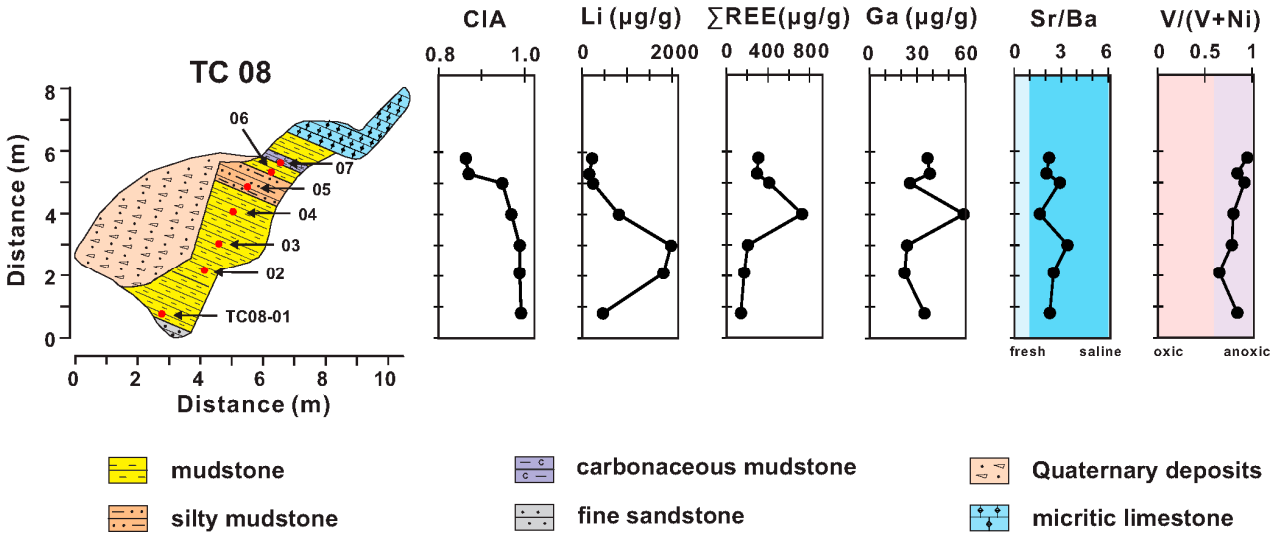


Figure 6. The geochemistry of trail trench TC08.

5. Discussion

5.1. The Origin and Deposit of Clays

Generally, there are two types of Li-rich clays according to their origins, e.g., the volcanic deposit and the weathering formation [3]. During the late Carboniferous to early Permian, there were no significant tectonic events or volcanic activities reported in the SCB (South China Block) [16–18]. Also, the parallel unconformity between the Huanglong Formation and the Liangshan Formation (i.e., the Li-rich deposit) indicates the erosion and weathering of the paleosurface. Thus, the clays in the Liangshan Formation formed due to the weathering of the bedrock instead of the hydrothermal alteration of volcanic sediments.

The Huanglong Formation under the Liangshan Formation is a carbonate deposit. However, given the field observations and the published references, sandy limestone, dolomite sandstone, lithic debris, and other impurities can be seen in the carbonates in the Huanglong Formation, which is under the Liangshan Formation [15,19]. During the weathering process, the carbonate is prone to being completely dissolved, especially in acid environments [26]. However, during the weathering of impurities in the carbonate (e.g., silicates), the mobile elements (e.g., K, Ca, Mg, and Na) are prone to being dissolved, but the poorly mobile elements (e.g., Al) are usually enriched in the weathering products (e.g., clays) [27]. Thus, the differential weathering of carbonate and silicate impurities in the Huanglong Formation may have caused the enrichment of clays in the Liangshan Formation. Moreover, because the high field strength elements, e.g., Zr, Hf, Nb, and Ta, are hardly transported or removed during weathering processes, the ratios of these elements in the weathering products are usually inherited from the bedrock [9]. In this study, the samples from weathering deposits and the underlying carbonate display the linear relationships of Zr and Hf, and Nb and Ta (Figure 7). Therefore, this suggests that the weathering of the underlying impure limestone provided the source of the materials deposited in the Liangshan Formation, similar to several reported cases [9,15,28].

According to the mineral composition analysis, the major secondary mineral in the Liangshan Formation is kaolinite, which is usually produced by the weathering of acid rocks (e.g., feldspar) and other weathering products (e.g., smectite) (Table 1) [28,29]. In samples TC08-01 to 04 and ZK1402-02 to 05, the kaolinite takes up more than 80% of the bulk samples. Such a large number of kaolinites indicates a high degree of weathering. Correspondingly, the CIA of the samples ranges from 84% to 99%, which also shows the high degree of weathering (Figures 4–6) [23]. Such a high degree of weathering generally happens in the supply-limited weathering regime, where there is a lack of fresh materials but it is under wet and hot climate conditions [30]. Therefore, this shows that the paleoclimate

conditions during the weathering stage are hot and wet, which corresponds to the reported paleotemperature during the late Carboniferous and early Permian in the SCB [31].

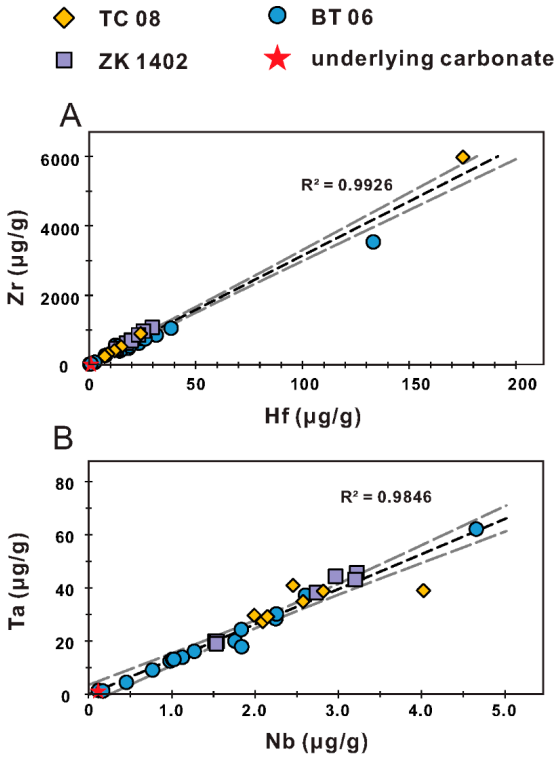


Figure 7. The plots of Zr versus Hf (**A**) and Ta versus Nb (**B**). The black dash lines are the best-fit lines, and the grey dash lines represent the boundaries of the fits with *p* less than 0.05.

Based on the XRD patterns, the Hinckley index (H.I.) of the samples that consist of more than 50% kaolinite was calculated (Figure S1) [24,25]. The H.I. was thought to indicate the crystallinity of the kaolin deposits, and a higher H.I. refers to more ordered structures [24,32]. The H.I. of samples BT06-09 to 13, TC08-01 to 04, and ZK1402-02 to 05 ranges from 0.3 to 1.6, and the H.I. values of most samples are higher than 1.0 which indicates that they are well ordered (Table 1). This also supports that there was a good weathering condition for kaolinite formation, although the kaolin disorder is influenced by multiple processes, such as weathering, sedimentary, diagenesis, and so on [24,25,32]. Moreover, some previous studies have showed that the Fe incorporated in the octahedral layers could reduce the degree of the kaolin orders [32], but there was no clear trend between the Fe content and H.I. in this study (Figure 8).

After the weathering stage, the residual minerals and the neo-formed clays probably remain in situ or are deposited in the nearby low land, because, as mentioned in Section 2.1, the study area was located in the coastal zone in the late Artinskian due to the sea level rising (Figure 1E). The ratio of Sr/Ba is thought of as an indicator of the salinity of the sedimentary environment, with <0.6 as fresh water, 0.6–1.0 as brackish water, and >1.0 as saline water [12,28]. Here, the Sr/Ba ratios of samples (except for ZK1402-01) from the Liangshan Formation range from 1.4 to 5.4 (Figures 4–6), which indicates that the study area was covered by brackish/saline water [28,33]. Furthermore, except for sample BT06-02, the V/(V + Ni) values of the samples from the Liangshan Formation are higher than 0.65 (Figures 4–6). The V/(V + Ni) is thought of as an indicator of the redox condition of the sedimentary environment, separated as <0.45 (oxic), 0.45–0.60 (dysoxic), 0.60–0.84 (suboxic), and >0.84 (anoxic) [34,35]. The V/(V + Ni) in the samples indicates the anoxic sedimentary environment here [35,36]. Thus, the sedimentary environment of the residual minerals and clays is predicted to be anoxic and still the land–sea interaction area [9,28,37].

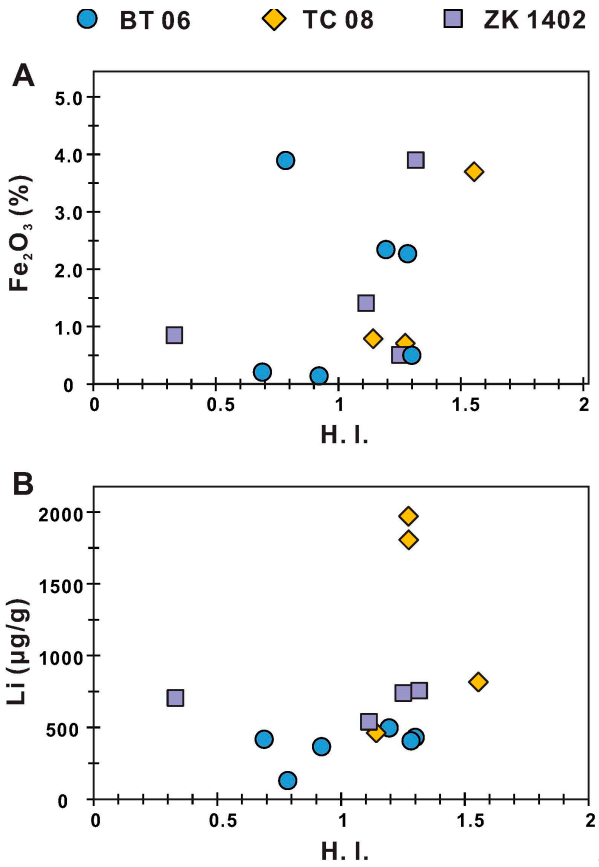


Figure 8. The relationship between Hinckley index (H.I.) and Fe_2O_3 content (**A**) and Li concentration (**B**). The H.I. calculation method is shown in Section 3.1 and Figure S1. Samples BT06-09 to 13, TC08-01 to 04, and ZK1402-02 to 05 are shown.

5.2. The Enrichment of Lithium

Lithium is the lightest metal element and alkali element. Li is an active element during surface weathering. To be specific, Li can be dissolved out during mineral dissolution and can also be adsorbed by secondary minerals, e.g., oxides and clays [38–42]. Thus, in this study, we predicted that the Li enrichments result from the weathering and deposition processes.

During the weathering stage, the Li dissolved out from the limestone in the Huanglong Formation provided the source of Li in the Li-rich deposits in the Liangshan Formation, given that Li can be leached out from carbonate using weak acid [43–45]. Meanwhile, the uptake of Li from the dissolved load by secondary minerals, especially the clays in the exchangeable pool or the lattices, has been observed widely in modern earth surfaces and water–rock interaction experiments [38–40,46–49]. Similarly, in the early Permian in this study area, Li was predicted to be taken by a large number of formed clays during weathering, so the Li was therefore enriched. Furthermore, the Li concentrations in the samples generally increase with the Al_2O_3 composition and CIA (Figure 9), which also indicates that the higher degree of weathering and more clay formation help Li enrichment. The principal component analysis (details in Supplementary Materials) shows that the major influencing factors of Li concentration are similar to Al_2O_3 concentration, CIA, clay content, and kaolinite content (Figures 10, S3 and S4).

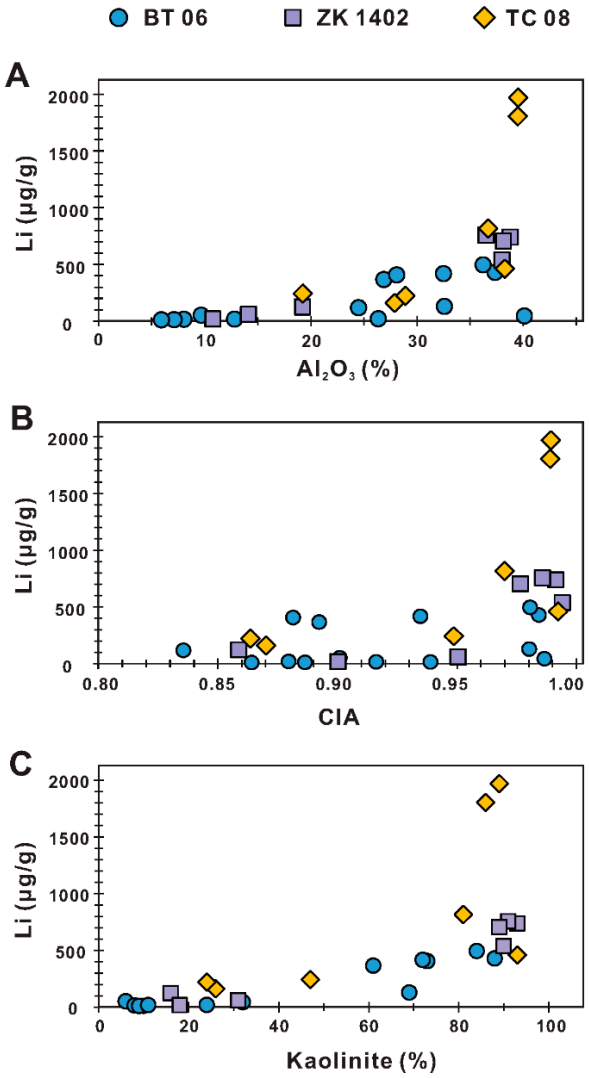


Figure 9. The relationships between Li and Al_2O_3 composition (**A**), CIA (**B**), and kaolinite composition (**C**).

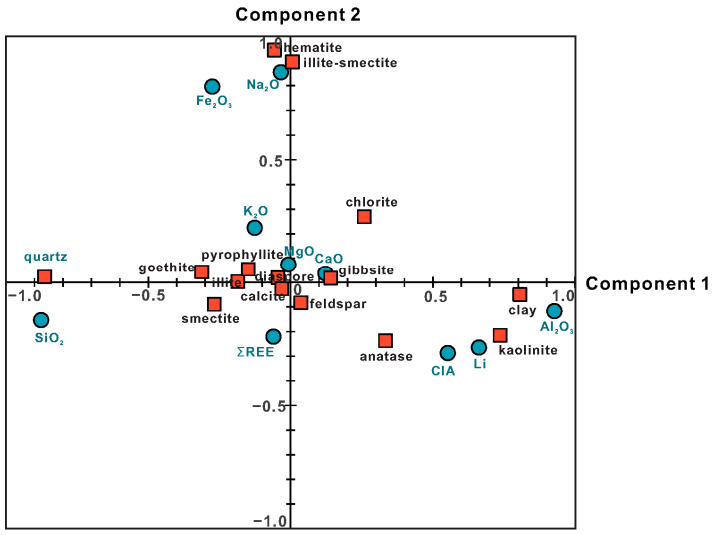


Figure 10. The influences of the first two components on variables based on PCA. The details on the PCA method are in the Supplementary Material.

According to the mineralogy analysis, kaolinite is the major clay mineral in the samples (Table 1). Also, there is a positive relationship between Li concentration and kaolinite composition in the samples (Figure 9). Although the samples also have some other minerals that may contain Li, such as illite, smectite, gibbsite, feldspar, and goethite [9], there is no correlation between these mineral compositions and Li concentration. Also, some Li-rich minerals reported in previous works are not found here, such as K–Mn-bearing ferricretes usually formed from Mn–ore minerals instead of weathering of impure carbonates [50]. There were no Li–smectite minerals either, e.g., swinefordite [51], hectorite [52], and saliotite [53], probably because the smectites were further weathered and transformed to kaolinite due to the wet climate [54]. Thus, the kaolinite is probably the main Li host mineral here. Although kaolinite is a 1:1 clay mineral whose cation exchange capacity (CEC) is lower than smectite and other 2:1 clay minerals [9,28,29], some water–rock interaction experiments suggest that the kaolinite can take the Li significantly and rapidly [49,55]. For example, when the initial Li concentration in the solution (pH 7; ~20 °C) is 10 and 75 μmol/L, the kaolinite can adsorb > 90% and ~60% Li from the solution, respectively, after 15 days [49]. An experiment by Zhang et al. (2021) [55] showed that the kaolinite adsorbed more than 70% of the Li from saline water after 165 days under pH ~8 and 25 °C conditions. In Figure 9C, there are two samples from TC08 with extremely high Li concentrations and around 90% kaolinite, which also indicates the large capability for kaolinite to take Li.

In addition, Li isotopes in previous studies have demonstrated that Li can both attach to the surface of the kaolinite via hydrogen bonds and also occupy the structural defects of the Al–O–Si skeleton [49]. However, so far, the Li coordination environments in clays cannot be determined directly [49]. In this study, there is no clear relationship between Li concentration and H.I., which indicates the crystallinity of kaolin deposits (Figure 8). This may imply that the Li is more likely to be attached to kaolinite via hydrogen bonds rather than occupying the Al–O–Si skeleton. However, as mentioned, the kaolin disorder is influenced by multiple processes [32]. Thus, more analyses may help to constrain the sites of Li in the kaolinite in further works, such as Li isotopes. Overall, during the weathering processes (late Carboniferous to early Permian), we predicted that the Li, which was dissolved out from underlying carbonate, was enriched through clay adsorption to attach to the kaolinite via hydrogen bonds or to occupy the structural sits.

As discussed, during the deposit stage, the study area was located in the land–sea interaction area (Section 5.1). Given that a few recent studies have suggested that oxide and clay minerals can take up Li from a dissolved load in the estuarine area [56,57], the clay may have further uptaken the Li from the brackish/saline water here. In other words, besides the Li from the underlying carbonate during the weathering stage, the Li from brackish/saline water during the deposit stage may have also contributed to the Li source in the Li-rich deposits in the Liangshan Formation. However, this hypothesis needs to be further confirmed with more evidence, such as the Li isotope composition of samples.

As mentioned in Section 2.2, there were coal-bearing layers in the study area of the Liangshan Formation, specifically in the location of BT06-14 based on observations in the field work and under the microscope. Also, layers of BT06-10 to 13 and TC08-07 were carbonaceous mudstone (Figure 2). Some studies have reported high-Li coals, such as in Jungar, Pingshuo, and Qinglong, China [58–61]. Most studies have shown that Li was mainly enriched in inorganic compositions, especially clays, such as kaolinite and illite [60,62,63]. Although, some studies have also reported high levels of Li in organic composition, the Li in organic composition was probably due to the redistribution from clays during diagenesis [64]. In this study, generally, the mudstone layers had higher Li concentrations than carbonaceous mudstone, while the silty mudstone and fine sandstone had lower Li concentrations (Figures 4–6). There was no significant relationship between Li concentrations and organic characteristics in the different layers. Thus, the organic matters (e.g., coals) were thought to have a minor effect on Li enrichment in this study.

Besides the Li enrichment, the samples from the Liangshan Formation also showed high ΣREE and Ga concentrations in ranges from 117 to 729 μg/g and 4.63 to 59.4 μg/g,

respectively (Figures 4–6). However, the ΣREE and Ga concentrations in samples BT06-01 (i.e., from Huanglong Formation) were only 56.1 and 1.11 μg/g (Tables 3 and 4). In addition, the RRE patterns (normalized by CI–chondrite, [22]) indicate the more significant enrichment of LREE (i.e., La–Eu) than HREE (i.e., Gd–Ho) (Figure 11). The co-enrichment of Li, REE, and Ga in the early Permian has been founded in the Sichuan and Guizhou Province in the SCB [10,13].

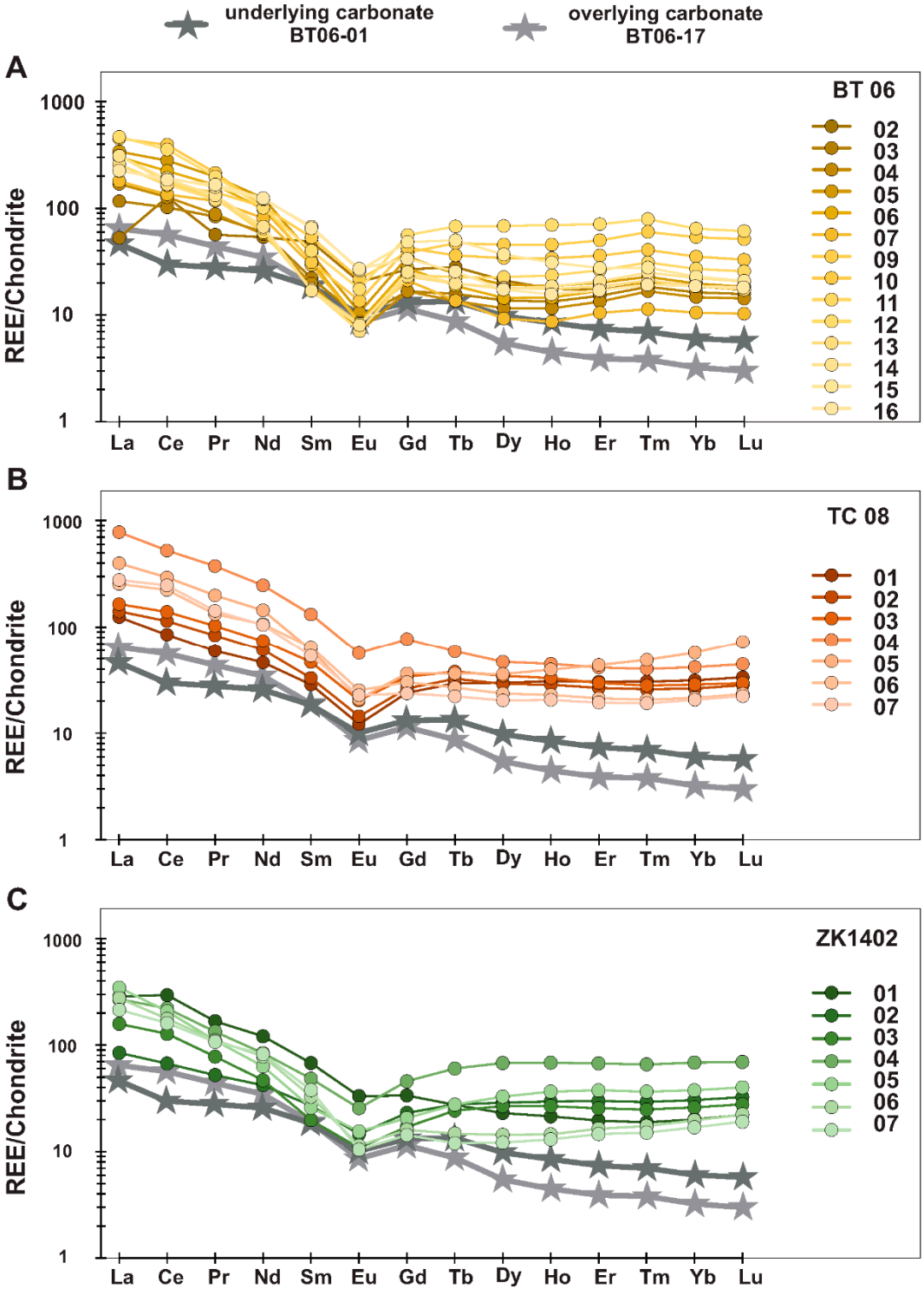


Figure 11. The normalized REE patterns of trail trenches BT06 (**A**) and TC08 (**B**) and drill core ZK1402 (**C**).

5.3. Implications on Prospecting of Bauxite-Related Li-Rich Deposits

Based on the results of this study and the published references, we summarize the common characteristics and the formation conditions of claystone-related Li-rich deposits here [3,9–11,13,28,37]. First, in view of stratigraphy, the Li-rich claystone deposits usually have parallel unconformity cover on the layer of carbonate (Section 2.2) [9,10,13]. The parallel unconformity indicates the paleo-weathering process, which is the key process of clay formation and Li enrichment (Sections 5.1 and 5.2). Second, in view of petrology and mineralogy, the underlying carbonate is usually impure carbonate, such as micritic limestone. The impure carbonate formation provided the source of lithium and other elements (e.g., Al and REE) for the clay formation and Li enrichment (Section 5.2), and the higher Li concentration in the underlying carbonate may have had an advantage for Li enrichment [28]. The Li-rich deposit is usually in the layer of claystone and mudstone, which mainly contains the secondary minerals (e.g., kaolinite, illite, smectite, and gibbsite) and the residual minerals (e.g., quartz) (Section 5.1) [3,11,28]. Third, in terms of the paleoclimate and palaeogeography, the Li-rich clay deposits were often formed in the anoxic, still, and flat land–sea interaction area [14,28]. More importantly, the area was in the coastal sea, which had experienced a cycle of regression (or uplift) and transgression, which provides the conditions for a series of weathering and sedimentary processes (Section 5.1). In addition, the paleoclimate of the weathering stage was predicted to be hot and wet, and the weathering was therefore the supply-limited regime, which benefits the clay formation and Li adsorption (Section 5.1) [30]. Thus, to prospect more Li-rich clay deposits in the SCB or even worldwide, the key indicators are parallel unconformity between clay deposits and impure carbonate, a wet and hot paleoclimate, a flat land–sea interaction area in the paleogeography, and a series of regressive (or uplift) and transgressive sea level changes.

Li-rich clay resources have not been widely used in industry yet due to their low concentration and complicated extraction method compared to Li-rich pegmatite and Li-rich brine [28]. So far, a few methods of Li leaching from Li-bearing clays have been developed, such as the mixed acid leaching method [65,66], the calcination acid method [67], and the calcination salt method [68], although these current methods still have some drawbacks, such as high cost, low extraction rates, and risk of environmental pollution [28]. However, because the demand for Li resources in industry is increasing rapidly, Li from clay-type Li deposits has big potential to be an important resource if more clay-type Li-rich deposits could be found and the extraction methods improved in the future.

6. Conclusions

This study demonstrated a Li-rich clay deposit with Li_2O content up to 0.3% in the Liangshan Formation in the upper Yangtze, South China Block. The Li-rich deposit was found in the mudstone and claystone layers. The results of the mineralogy and geochemistry analysis of the samples from the Li-rich deposit and its underlying and overlying layers showed that the major Li-host mineral is clay, especially kaolinite. In addition, the clay formation and Li enrichment are related to the weathering of the underlying impure limestone and sedimentary in the anoxic, still and flat land–sea interaction area in the upper Yangtze in the SCB. The Li was sourced from underlying impure limestone during the weathering stage and brackish/saline water during the deposit stage. Furthermore, the climate conditions during the weathering stage were predicted to be hot and warm. Thus, we propose that there is big potential to find more clay-type Li-rich deposits with key indicators such as parallel unconformity between bauxite and impure carbonate, wet and hot paleoclimate, flat land–sea interaction areas in the paleogeography, and a series of regressive (or uplift) and transgressive sea-level changes. Because of the high demand for Li in industries, clay-type Li-rich deposits have the potential to be a supply of Li resources in the future, especially if the extraction methods could be improved.

Supplementary Materials: The following supporting information can be downloaded at: https://www.mdpi.com/article/10.3390/min14070735/s1, Figure S1: XRD-based determination of the Hinckley index. Figure S2: Box plots of concentrations of Li, Al_2O_3, and total REE in samples from the Liangshan Formation. Figure S3: Scree plot of PCA. Figure S4: Plots of influences of different components on variables. Table S1: The lithology of the stratigraphic succession in the study area. Text S1: Principal component analysis and factor analysis.

Author Contributions: Conceptualization, Y.G.; methodology, Y.G.; investigation, Y.G. and C.-Y.L.; resources, Y.G., Y.L., L.L., M.X., B.Y., Z.Z., Y.Z., X.-R.Y., L.Y. and Y.X.; data curation, Y.G.; writing—original draft preparation, Y.G. and C.-Y.L.; writing—review and editing, Y.L., L.L., M.X., B.Y., Z.Z., Y.Z., X.-R.Y., L.Y. and Y.X.; supervision, Y.G.; project administration, Y.G.; funding acquisition, Y.G. All authors have read and agreed to the published version of the manuscript.

Funding: This research was funded by (1) the Seventh Geological Brigade of Hubei Geological Bureau, project "The genetic mechanism of typical brittle minerals in the shales of Gufeng and Dalong formations of Permian in western Hubei and their influence on reservoirs", grant number "DQKJ2023-2", (2) Hubei geological survey funding, project "Lithium resource prospecting in Xiping area, Changyang County", grant number "JKKQ-ZFCG-20230431", and (3) the Comprehensive Geological Regionalization of Hubei Province (Western Hubei), grant number "KCDZ2024-30".

Data Availability Statement: The data presented in the study are included in the article, further inquiries can be directed to the corresponding author.

Acknowledgments: We thank the helpful suggestions from Quanxu Zhang in the sample collection and manuscript preparation. We thank the three reviewers for their constructive comments.

Conflicts of Interest: The authors declare no conflicts of interest.

References

1. Xie, J.; Lu, Y.-C. A retrospective on lithium-ion batteries. *Nat. Commun.* **2020**, *11*, 2499. [CrossRef]
2. Eswara Prasad, N.; Gokhale, A.A.; Wanhill, R.J.H. *Aluminum-Lithium Alloys*; Elsevier: Amsterdam, The Netherlands, 2014; ISBN 9780124016989.
3. Ling, K.; Wen, H.; Han, T.; Lu, Z.; Cui, Y.; Luo, C.; Yu, W. Lithium-rich claystone in Pingguo area, Guangxi, southwest China: Precursor kaolinite controls lithium enrichment. *Miner. Depos.* **2024**, *59*, 329–340. [CrossRef]
4. Vikström, H.; Davidsson, S.; Höök, M. Lithium availability and future production outlooks. *Appl. Energy* **2013**, *110*, 252–266. [CrossRef]
5. Kesler, S.E.; Gruber, P.W.; Medina, P.A.; Keoleian, G.A.; Everson, M.P.; Wallington, T.J. Global lithium resources: Relative importance of pegmatite, brine and other deposits. *Ore Geol. Rev.* **2012**, *48*, 55–69. [CrossRef]
6. Benson, T.R.; Coble, M.A.; Rytuba, J.J.; Mahood, G.A. Lithium enrichment in intracontinental rhyolite magmas leads to Li deposits in caldera basins. *Nat. Commun.* **2017**, *8*, 270. [CrossRef]
7. Verley, C.G.; Geo, P. *Updated and Reclassified Lithium Resources, Sonora Lithium Project, Sonora, Mexico*; Amerlin Exploration Services Ltd.: Richmond, BC, Canada, 2014.
8. Bowell, R.J.; Lagos, L.; de los Hoyos, C.R.; Declercq, J. Classification and Characteristics of Natural Lithium Resources. *Elements* **2020**, *16*, 259–264. [CrossRef]
9. Wen, H.; Luo, C.; Du, S.; Yu, W.; Gu, H.; Ling, K.; Cui, Y.; Li, Y.; Yang, J. Carbonate-hosted clay-type lithium deposit and its prospecting significance. *Chin. Sci. Bull.* **2020**, *65*, 53–59. [CrossRef]
10. Jin, Z.; Liu, L.; Hunag, Z.; Liu, C.; Zheng, M.; Gu, J.; Zou, L.; Wang, L. Occurrence state, enrichment mechanism and resource potential of rare earth, rare metal and rare-scattered elements in ore-bearing rocks in the Wuchuan-Zheng'an-Daozhen bauxite deposit, Guizhou Province. *Acta Geol. Sinca* **2019**, *93*, 2847–2861. [CrossRef]
11. Tang, B.; Fu, Y.; Yan, S.; Chen, P.-W.; Cao, C.; Guo, C.; Wu, P.; Long, Z.; Long, K.-S.; Wang, T.-S.; et al. The source, host minerals, and enrichment mechanism of lithium in the Xinmin bauxite deposit, northern Guizhou, China: Constraints from lithium isotopes. *Ore Geol. Rev.* **2022**, *141*, 104653. [CrossRef]
12. Jia, Y.; Yu, W.; Wen, H.; Luo, C.; Yang, G.; Yang, Y.; Cui, Y. Geochemical Characteristics and Sedimentary Environment of Li-rich Clay Rocks at the Southern Margin of the Central Yunnan Basin. *Acta Sedimentol. Sin.* **2023**, *41*, 170–182. [CrossRef]
13. Yue, X.; Jia, Z.; Luo, S.; Tan, H.; Liang, B.; Luo, L. Lithium, Rare Earth and Gallium-Rich Layers Found in the Lower Permian Liangshan Formation, Panzhihua, Sichuan. *Multipurp. Util. Miner. Resour.* **2023**, *4*, 122–126. [CrossRef]
14. Ling, K.; Wen, H.; Zhang, Q.; Luo, C.; Gu, H.; Du, S.; Yu, W. Super-enrichment of lithium and niobium in the upper Permian Heshan Formation in Pingguo, Guangxi, China. *Sci. China Earth Sci.* **2021**, *64*, 753–772. [CrossRef]
15. Wang, X.; Qie, W.; Sheng, Q.; Qi, Y.; Wang, Y.; Liao, Z.; Shen, S.; Ueno, K. Carboniferous and Lower Permian sedimentological cycles and biotic events of South China. *Geol. Soc. Lond. Spec. Publ.* **2013**, *376*, 33–46. [CrossRef]

16. Hou, Z.; Shen, S.; Henderson, C.M.; Yuan, D.; Zhang, Y.; Fan, J. Cisuralian (Early Permian) paleogeographic evolution of South China Block and sea-level changes: Implications for the global Artinskian Warming Event. *Palaeogeogr. Palaeoclimatol. Palaeoecol.* **2023**, *613*, 111395. [CrossRef]
17. Wang, X.; Hu, K.; Qie, W.; Sheng, Q.; Chen, B.; Lin, W.; Yao, L.; Wang, Q.; Qi, Y.; Chen, J.; et al. Carboniferous integrative stratigraphy and timescale of China. *Sci. China Earth Sci.* **2019**, *62*, 135–153. [CrossRef]
18. Shen, S.; Zhang, H.; Zhang, Y.; Yuan, D.; Chen, B.; He, W.; Mu, L.; Lin, W.; Wang, W.; Chen, J.; et al. Permian integrative stratigraphy and timescale of China. *Sci. China Earth Sci.* **2019**, *62*, 154–188. [CrossRef]
19. Li, W.; Zhang, Z.; Dang, L. Depositional systems and evolution of the Upper Carboniferous Huanglong Formation in the eastern Sichuan Basin. *Pet. Explor. Dev.* **2011**, *38*, 400–409. [CrossRef]
20. Wang, K.; Hu, S.; Li, W.; Liu, W.; Huang, Q.; Ma, K.; Shi, S. Depositional System of the Carboniferous Huanglong Formation, Eastern Sichuan Basin: Constraints from Sedimentology and Geochemistry. *Acta Geol. Sin. Engl. Ed.* **2016**, *90*, 1795–1808. [CrossRef]
21. Mei, M.; Ma, Y.; Deng, J.; Meng, Q.; Yi, D.; Li, D. Late Paleozoic sequence-stratigraphic frameworks and sea level changes in Dianqiangui Basin and its adjacent areas with systematic revision of regional unconformities. *J. China Univ. Geosci.* **2004**, *15*, 55–68.
22. Sun, S.-S.; McDonough, W.F. Chemical and isotopic systematics of oceanic basalts: Implications for mantle composition and processes. *Geol. Soc. Lond. Spec. Publ.* **1989**, *42*, 313–345. [CrossRef]
23. Nesbitt, H.W.; Young, G.M. Early proterozoic climates and plate motions inferred from major element chemistry of lutites. *Nature* **1982**, *299*, 715–717. [CrossRef]
24. Hinckley, D.N. Variability in "crystallinity" Values among the Kaolin Deposits of the Coastal Plain of Georgia and South Carolina. *Clays Clay Technol. (Natl. Conf. Clays Clay Technol.)* **1962**, *11*, 229–235. [CrossRef]
25. Dill, H.G. Kaolin: Soil, rock and ore. *Earth-Science Rev.* **2016**, *161*, 16–129. [CrossRef]
26. Meybeck, M. Global chemical weathering of surficial rocks estimated from river dissolved loads. *Am. J. Sci.* **1987**, *287*, 401–428. [CrossRef]
27. Gislason, S.R.; Oelkers, E.H. Silicate Rock Weathering and the Global Carbon Cycle. In *Frontiers in Geochemistry*; John Wiley & Sons, Ltd: Chichester, UK, 2011; pp. 84–103.
28. Wu, Z. Advance review on occurrence state and leaching of lithium in sedimentary bauxite (aluminum) deposits, China. *Ore Geol. Rev.* **2024**, *164*, 105851. [CrossRef]
29. *Velde B Origin and Mineralogy of Clays*; Springer: Berlin/Heidelberg, Germany, 1995; ISBN 3-540-58012-3.
30. West, A.J.; Galy, A.; Bickle, M. Tectonic and climatic controls on silicate weathering. *Earth Planet. Sci. Lett.* **2005**, *235*, 211–228. [CrossRef]
31. Wang, R.; Wang, Q.; Huang, Y.; Yang, S.; Liu, X.; Zhou, Q. Combined tectonic and paleogeographic controls on the genesis of bauxite in the Early Carboniferous to Permian Central Yangtze Island. *Ore Geol. Rev.* **2018**, *101*, 468–480. [CrossRef]
32. Brindley, G.W.; Kao, C.-C.; Harrison, J.L.; Lipsicas, M.; Raythatha, R. Relation Between Structural Disorder and Other Characteristics of Kaolinites and Dickites. *Clays Clay Miner.* **1986**, *34*, 239–249. [CrossRef]
33. Wei, W.; Algeo, T.J. Elemental proxies for paleosalinity analysis of ancient shales and mudrocks. *Geochim. Cosmochim. Acta* **2020**, *287*, 341–366. [CrossRef]
34. Hatch, J.R.; Leventhal, J.S. Relationship between inferred redox potential of the depositional environment and geochemistry of the Upper Pennsylvanian (Missourian) Stark Shale Member of the Dennis Limestone, Wabaunsee County, Kansas, U.S.A. *Chem. Geol.* **1992**, *99*, 65–82. [CrossRef]
35. Jin, C.; Liao, Z.; Lash, G.G. High-frequency redox variation across the Ordovician–Silurian transition, South China. *Palaeogeogr. Palaeoclimatol. Palaeoecol.* **2021**, *566*, 110218. [CrossRef]
36. Rimmer, S.M. Geochemical paleoredox indicators in Devonian–Mississippian black shales, Central Appalachian Basin (USA). *Chem. Geol.* **2004**, *206*, 373–391. [CrossRef]
37. Cui, Y.; Luo, C.; Xu, L.; Zhang, H.; Deng, M.; Gu, H.; Meng, Y.; Qin, C.; Wen, H. Weathering origin and enrichment of lithium in clay rocks of the Jiujialu Formation, Central Guizhou Province, Southwest China. *Bull. Mineral. Geochem.* **2018**, *37*, 696–704.
38. Dellinger, M.; Gaillardet, J.; Bouchez, J.; Calmels, D.; Louvat, P.; Dosseto, A.; Gorge, C.; Alanoca, L.; Maurice, L. Riverine Li isotope fractionation in the Amazon River basin controlled by the weathering regimes. *Geochim. Cosmochim. Acta* **2015**, *164*, 71–93. [CrossRef]
39. Pogge von Strandmann, P.A.E.; Kasemann, S.A.; Wimpenny, J.B. Lithium and Lithium Isotopes in Earth's Surface Cycles. *Elements* **2020**, *16*, 253–258. [CrossRef]
40. Dellinger, M.; Gaillardet, J.Ô.; Bouchez, J.; Calmels, D.; Galy, V.; Hilton, R.G.; Louvat, P.; France-Lanord, C. Lithium isotopes in large rivers reveal the cannibalistic nature of modern continental weathering and erosion. *Earth Planet. Sci. Lett.* **2014**, *401*, 359–372. [CrossRef]
41. Pogge von Strandmann, P.A.E.; Frings, P.J.; Murphy, M.J. Lithium isotope behaviour during weathering in the Ganges Alluvial Plain. *Geochim. Cosmochim. Acta* **2017**, *198*, 17–31. [CrossRef]
42. Li, W.; Liu, X.M.; Chadwick, O.A. Lithium isotope behavior in Hawaiian regoliths: Soil-atmosphere-biosphere exchanges. *Geochim. Cosmochim. Acta* **2020**, *285*, 175–192. [CrossRef]

43. Pogge von Strandmann, P.A.E.; Schmidt, D.N.; Planavsky, N.J.; Wei, G.; Todd, C.L.; Baumann, K.H. Assessing bulk carbonates as archives for seawater Li isotope ratios. *Chem. Geol.* **2019**, *530*, 119338. [CrossRef]
44. Cao, C.; Liu, X.M.; Wang, X.K.; Chen, J. Effective use of limestones to reconstruct seawater Li isotope compositions—A community standard proposal. *Chem. Geol.* **2023**, *626*, 121441. [CrossRef]
45. Liu, C.-Y.; Pogge von Strandmann, P.A.E.; Tarbuck, G.; Wilson, D.J. Experimental Investigation of Oxide Leaching Methods for Li Isotopes. *Geostand. Geoanalytical Res.* **2022**, *46*, 493–518. [CrossRef] [PubMed]
46. Pogge von Strandmann, P.A.E.; Fraser, W.T.; Hammond, S.J.; Tarbuck, G.; Wood, I.G.; Oelkers, E.H.; Murphy, M.J. Experimental determination of Li isotope behaviour during basalt weathering. *Chem. Geol.* **2019**, *517*, 34–43. [CrossRef]
47. Hindshaw, R.S.; Tosca, R.; Goût, T.L.; Farnan, I.; Tosca, N.J.; Tipper, E.T. Experimental constraints on Li isotope fractionation during clay formation. *Geochim. Cosmochim. Acta* **2019**, *250*, 219–237. [CrossRef]
48. Wimpenny, J.; Colla, C.A.; Yu, P.; Yin, Q.Z.; Rustad, J.R.; Casey, W.H. Lithium isotope fractionation during uptake by gibbsite. *Geochim. Cosmochim. Acta* **2015**, *168*, 133–150. [CrossRef]
49. Li, W.; Liu, X.M. Experimental investigation of lithium isotope fractionation during kaolinite adsorption: Implications for chemical weathering. *Geochim. Cosmochim. Acta* **2020**, *284*, 156–172. [CrossRef]
50. Dill, H.G. The "chessboard" classification scheme of mineral deposits: Mineralogy and geology from aluminum to zirconium. *Earth-Sci. Rev.* **2010**, *100*, 1–420. [CrossRef]
51. Tien, P.-L.; Leavens, P.B.; Nelen, J.A. Swinefordite, A Dioctahedral-Trioctahedral Li-Rich Member of the Smectite Group from Kings Mountain, North Carolina. *Am. Mineral.* **1975**, *60*, 540–547.
52. Zhang, J.; Zhou, C.H.; Petit, S.; Zhang, H. Hectorite: Synthesis, modification, assembly and applications. *Appl. Clay Sci.* **2019**, *177*, 114–138. [CrossRef]
53. Goffé, B.; Baronnet, A.; Morin, G. La saliotite, interstratifié régulier 1:1 cookéite/paragonite. Nouveau phyllosilicate du métamorphisme de haute pression et basse température. *Eur. J. Mineral.* **1994**, *6*, 897–912. [CrossRef]
54. Hong, H.; Churchman, G.J.; Gu, Y.; Yin, K.; Wang, C. Kaolinite–smectite mixed-layer clays in the Jiujiang red soils and their climate significance. *Geoderma* **2012**, *173–174*, 75–83. [CrossRef]
55. Zhang, X.; Saldi, G.D.; Schott, J.; Bouchez, J.; Kuessner, M.; Montouillout, V.; Henehan, M.; Gaillardet, J. Experimental constraints on Li isotope fractionation during the interaction between kaolinite and seawater. *Geochim. Cosmochim. Acta* **2021**, *292*, 333–347. [CrossRef]
56. Liu, C.-Y.; Wilson, D.J.; Hathorne, E.C.; Xu, A.; Pogge von Strandmann, P.A.E. The influence of river-derived particles on estuarine and marine elemental cycles: Evidence from lithium isotopes. *Geochim. Cosmochim. Acta* **2023**, *361*, 183–199. [CrossRef]
57. Yang, C.; Yang, S.; Vigier, N. Li isotopic variations of particulate non-silicate phases during estuarine water mixing. *Geochim. Cosmochim. Acta* **2023**, *354*, 229–239. [CrossRef]
58. Sun, B.; Zeng, F.; Moore, T.A.; Rodrigues, S.; Liu, C.; Wang, G. Geochemistry of two high-lithium content coal seams, Shanxi Province, China. *Int. J. Coal Geol.* **2022**, *260*, 104059. [CrossRef]
59. Seredin, V.V.; Dai, S.; Sun, Y.; Chekryzhov, I.Y. Coal deposits as promising sources of rare metals for alternative power and energy-efficient technologies. *Appl. Geochem.* **2013**, *31*, 1–11. [CrossRef]
60. Zhang, S.; Xiu, W.; Sun, B.; Liu, Q. Provenance of multi-stage volcanic ash recorded in the Late Carboniferous coal in the Jungar Coalfield, North China, and their contribution to the enrichment of critical metals in the coal. *Int. J. Coal Geol.* **2023**, *273*, 104265. [CrossRef]
61. Liu, B.; Lin, M. Enrichment Mechanism and Material Sources of Lithium in Li-Bearing Coal Seam No.9 from Pingshuo Mining District of Shanxi Province. *Coal Technol.* **2015**, *34*, 115–117.
62. Finkelman, R.B.; Palmer, C.A.; Wang, P. Quantification of the modes of occurrence of 42 elements in coal. *Int. J. Coal Geol.* **2018**, *185*, 138–160. [CrossRef]
63. Wang, X.; Wang, X.; Pan, Z.; Pan, W.; Yin, X.; Chai, P.; Pan, S.; Yang, Q. Mineralogical and geochemical characteristics of the Permian coal from the Qinshui Basin, northern China, with emphasis on lithium enrichment. *Int. J. Coal Geol.* **2019**, *214*, 103254. [CrossRef]
64. Jiu, B.; Huang, W.; Spiro, B.; Hao, R.; Mu, N.; Wen, L.; Hao, H. Distribution of Li, Ga, Nb, and REEs in coal as determined by LA-ICP-MS imaging: A case study from Jungar coalfield, Ordos Basin, China. *Int. J. Coal Geol.* **2023**, *267*, 104184. [CrossRef]
65. Zhang, Y.; Zhang, J.; Wu, L.; Tan, L.; Xie, F.; Cheng, J. Extraction of lithium and aluminium from bauxite mine tailings by mixed acid treatment without roasting. *J. Hazard. Mater.* **2021**, *404*, 124044. [CrossRef] [PubMed]
66. Wu, L.; Zhang, J.; Huang, Z.; Zhang, Y.; Xie, F.; Zhang, S.; Fan, H. Extraction of lithium as lithium phosphate from bauxite mine tailings via mixed acid leaching and chemical precipitation. *Ore Geol. Rev.* **2023**, *160*, 105621. [CrossRef]
67. Gu, H.; Guo, T.; Wen, H.; Luo, C.; Cui, Y.; Du, S.; Wang, N. Leaching efficiency of sulfuric acid on selective lithium leachability from bauxitic claystone. *Miner. Eng.* **2020**, *145*, 106076. [CrossRef]
68. Zhu, L.; Gu, H.; Wen, H.; Yang, Y. Lithium extraction from clay-type lithium resource using ferric sulfate solutions via an ion-exchange leaching process. *Hydrometallurgy* **2021**, *206*, 105759. [CrossRef]

Disclaimer/Publisher's Note: The statements, opinions and data contained in all publications are solely those of the individual author(s) and contributor(s) and not of MDPI and/or the editor(s). MDPI and/or the editor(s) disclaim responsibility for any injury to people or property resulting from any ideas, methods, instructions or products referred to in the content.